Available online at www.sciencedirect.com
SCIENCE DIRECT®
Precambrian Research 122 (2003) 253–273
Precambrian Research
www.elsevier.com/locate/precamres

Granulite-facies metamorphism in the Punggi area, northeastern Yeongnam Massif, Korea and its tectonic implications for east Asia

Yong Wan Kwon [a,*], Chang Whan Oh [b], Hyung Shik Kim [a,1]

[a] *Department of Earth and Environmental Sciences, Korea University, 136-701 Seoul, South Korea*
[b] *Department of Earth and Environmental Sciences, Chonbuk University, Chonju, South Korea*

Received 30 October 2001; received in revised form 24 July 2002; accepted 29 July 2002

Abstract

In the Punggi area of the northeastern part of the Yeongnam Massif, one of Precambrian basement terrains in Korean Peninsular, the metamorphic grade increases from the amphibolite- to the granulite-facies zones towards the southeast. The boundary of the granulite-facies zone is defined by the orthopyroxene (Opx)-In reaction in metabasites. As metamorphic grade increases across the Opx-In isograd, the mineral assemblage in calcic metabasites is changed from clinopyroxene-amphibole-plagioclase to orthopyroxene-clinopyroxene-amphibole-plagioclase, and that in alkali metabasites from garnet-orthoamphibole-plagioclase to garnet-orthopyroxene-plagioclase. The metamorphic rocks in the granulite-facies zone were overprinted by upper amphibolite-facies retrograde metamorphism. During retrograde metamorphism, cordierite and spinel formed in the migmatitic gneiss. The *P–T* conditions of granulite-facies metamorphism are 767–815 °C and 6.0–8.4 kb and the *P–T* conditions for the retrograde stage are 595–707 °C/4.7–6.4 kb. A U–Pb zircon age of 1904 ± 9 Ma has been obtained from a garnet granitic gneiss and is inferred to date the emplacement of its precursor. This is consistent with the intrusion age of precursors to most orthogneisses in other parts of the Yeongnam Massif. The same sample has yielded a Sm–Nd whole rock-garnet age of 617 ± 38 Ma, which is inferred to represent a late Proterozoic metamorphic event of upper amphibolite facies.

Keywords: Yeongnam Massif; Granulite-facies metamorphism; Orthopyroxene; U–Pb zircon age; Sm–Nd whole rock-garnet age

1. Introduction

In the southern part of Korean Peninsula, there are two Precambrian metamorphic basement terrains, which are separated by the Phanerozoic Ogcheon Belt: the Gyeonggi Massif and the Yeongnam (or Sobaegsan) Massif (Fig. 1). Since it has been recently proposed that the Dabie–Sulu collision belt in China may extend into the Korean Peninsula (Yin and Nie, 1993; Ernst and Liou, 1995; Chang, 1996; Ree et al., 1996), it has been a critical issue whether these Precambrian massifs are parts of a single massif belonging to the North China (Sino-Korean) Craton or two separate massifs. Kim et al. (1992) suggested that the Yeongnam Massif belongs to the South China (Yangtze) Craton and the Gyeonggi Massif to the North China Craton. However, Cluzel et al. (1991) and Yin and Nie (1993) suggested just the opposite. Alternatively, Cheong et al. (2000) and Park et al. (2000) proposed that two massifs are parts of the North China Craton. Although several models suggested for the tectonic relationship between northeast China

* Corresponding author. Fax: +82-2-3290-3560.
E-mail address: kwonyw@korea.ac.kr (Y.W. Kwon).
[1] Deceased.

0301-9268/02/$ – see front matter
PII: S0301-9268(02)00214-0

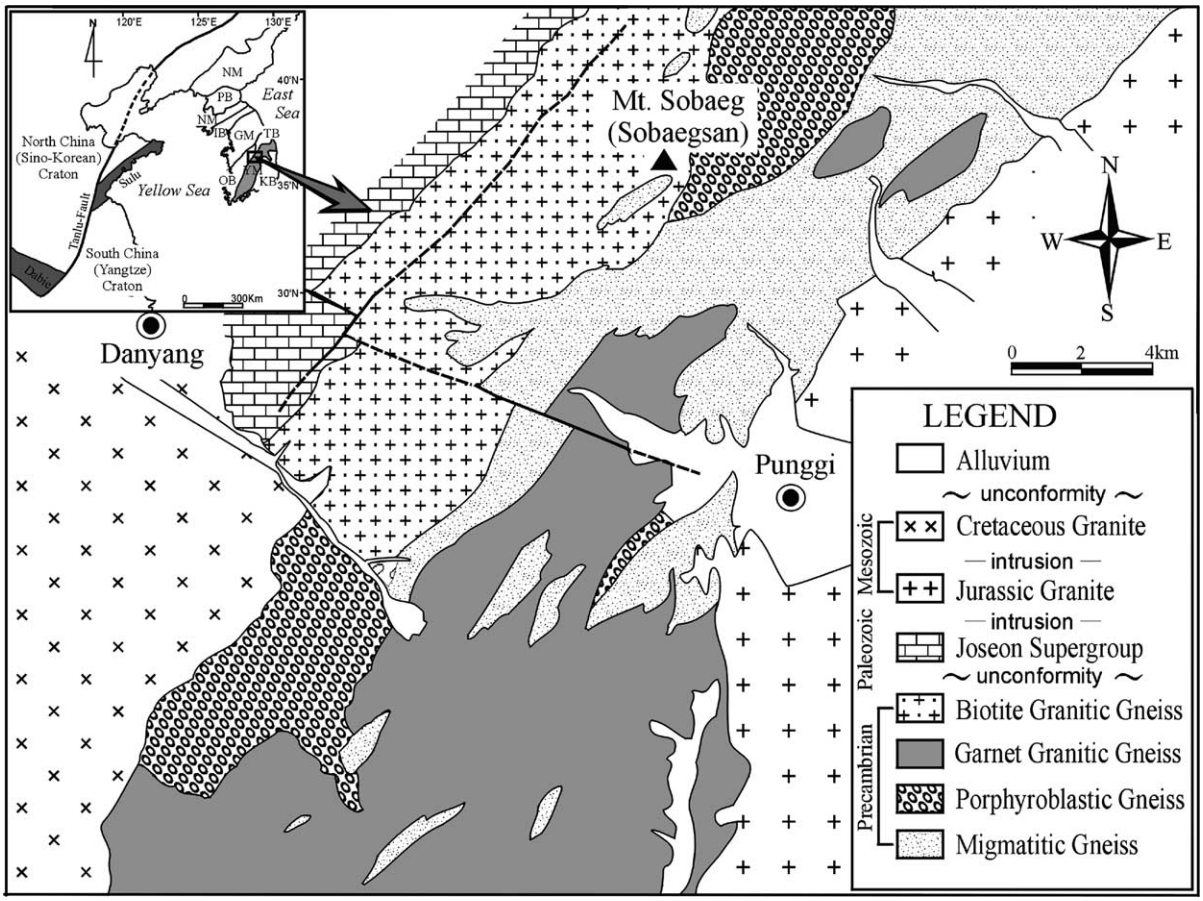

Fig. 1. Geological map of the study area, modified from 1:50,000 geologic maps of Danyang (Won and Lee, 1967), Sangkumgok (Shin and Choi, 1968) and Punggi (Lee et al., 1989) areas. The inset figure shows various tectonic provinces in east Asia. NM, Nangrim Massif; GM, Gyeonggi Massif; YM, Yeongnam Massif; PB, Pyeongnam basin; OB, Ogcheon metamorphic belt; IB, Imjingang belt; TB, Taebaegsan basin; KB, Kyeongsang basin.

and Korean Peninsula, the relationship is still obscure because of the lack of petrological and geochronological data for the Korean Peninsula. In particular, only a few petrological and geochronological studies on the Yeongnam Massif are available. Therefore, to elucidate the tectonic relationship between China and Korea, it is important to study the Yeongnam Massif.

The Yeongnam Massif had earlier been thought to have undergone upper amphibolite-facies peak metamorphism, followed by an amphibolite-facies overprint and then by the greenschist-facies retrogression (Lee et al., 1981; Song and Lee, 1989). However, recently, granulite-facies metamorphism was also reported from: (a) the southern part of the massif (800 °C and 3.5–6 kb, at 1.8 Ga; Kim, 1999; Song, 1999) and (b) the northeastern part of the massif (730–870 °C and 4.8–6.8 kb, unknown age; Kim and Cho, 1999, 2003; Yi, 2000). Evidence for granulite-facies metamorphism was also reported from the Hwacheon (800–850 °C and 7–10 kb, at 1.87 Ga; Lee et al., 2000) and Odaesan areas (776–798 °C and 5.4–7.4 kb, unknown age; Kwon et al., 1997) in the Gyeonggi Massif.

In the North China Craton, granulite-facies metamorphism at 1.8 Ga is common and generally no younger metamorphic event is prominent (Zhai et al., 2000). On the other hand, in the Sulu collisional region between North and South China cratons, granulite-facies metamorphism occurred during isothermal

decompression following 240–210 Ma ultrahigh-pressure metamorphism (Wang et al., 1993; Zhang et al., 1995; Yao et al., 2000). Granulite-facies metamorphism is common in northeast Asia and can be an important key to understand tectonic relationship between Korea and China.

This contribution documents the metamorphic evolution of previously unstudied granulite-facies granitic gneiss, metabasites and migmatites from the Punggi area (northeastern Yeongnam Massif) including *P–T* conditions and the timing of metamorphism. In addition the results of this study are compared with the granulite-facies metamorphism in other parts of the Yeongnam Massif, as well as the Gyeonggi Massif and the North and South China cratons in order to interpret the tectonic relationship between Korea and China.

2. Geological outline and metamorphic zones

In the Punggi area, the Yeongnam Massif is bounded to the NW by the Paleozoic Joseon Supergroup and was intruded by Mesozoic granites to the east and west (Fig. 1). The boundary between the Yeongnam Massif and the Joseon Supergroup is defined primarily by an unconformity and locally by a semi-brittle ductile shear zone (Kwon et al., 1995). The study area mainly comprises migmatitic gneiss, porphyroblastic gneiss, garnet granitic gneiss and biotite granitic gneiss. Metabasites occur as enclaves in garnet granitic gneiss and as small pods and boudins in migmatitic gneiss (Fig. 2).

The migmatitic gneiss shows a banded and stromatic structure and comprises quartz, plagioclase, perthite, biotite and muscovite with minor garnet, sillimanite, cordierite, spinel, corundum and ilmenite. Reddish brown biotite occurs as flakes that define the foliation together with muscovite, and greenish brown secondary biotite replaces garnet along cracks and fractures. Garnet grains are 2–3 mm in diameter and contain reddish brown biotite inclusions. Some garnet porphyroblasts are embayed by cordierite. Cordierite is poikiloblastic and contains inclusions of quartz, spinel, sillimanite and ilmenite (Fig. 3A). The whole rock composition of cordierite-bearing migmatitic gneiss has higher Al_2O_3, total FeO, MgO and K_2O than cordierite-free migmatitic gneiss (Table 1).

The porphyroblastic gneiss is characterized by porphyroblasts of perthite with diameters of 2–3 cm. The matrix of the porphyroblastic gneiss mainly comprises of quartz, plagioclase and biotite with minor hornblende and epidote.

The garnet granitic gneiss is generally massive. It displays weak foliation and contains xenoliths of migmatitic gneiss and enclaves of metabasite. Garnet, K-feldspar, biotite, plagioclase, and quartz occur as major minerals with minor prismatic sillimanite and ilmenite. Garnet porphyroblasts are about 1 cm in

Table 1
Representative whole rock compositions of gneisses and metabasites

	Rock					
	Mig Gn	Mig Gn*	Grt Gr Gn	Bt Gr Gn	Mb-1	Mb-2
SiO_2	69.98	42.64	68.04	68.58	48.03	50.86
Al_2O_3	15.01	25.69	14.96	15.09	14.83	19.42
Fe_2O_3**	4.55	14.74	6.19	6.54	13.73	9.51
TiO_2	0.80	1.36	0.70	0.61	0.86	0.92
MnO	0.05	0.12	0.08	0.08	0.19	0.06
CaO	3.02	1.34	3.62	1.59	12.67	6.49
MgO	1.83	5.86	2.25	2.03	7.79	4.80
K_2O	1.92	3.17	1.43	2.76	0.20	2.05
Na_2O	2.64	1.30	1.93	2.00	0.33	2.96
P_2O_5	0.06	0.08	0.03	0.09	0.08	0.83
LOI	0.00	1.63	0.58	0.65	0.46	0.42
Total	99.85	97.93	99.82	100.01	99.17	98.30

Mig Gn, Migmatitic Gneiss; Grt Gr Gn, Garnet Granitic Gneiss; Bt Gr Gn, Biotite Granitic Gneiss; Mb-1, Ca-rich metabasite; Mb-2, alkali metabasite containing orthopyroxene. Mig Gn*, cordierite bearing migmatitic gneiss; Fe_2O_3**, total Fe oxides; LOI, loss on ignition.

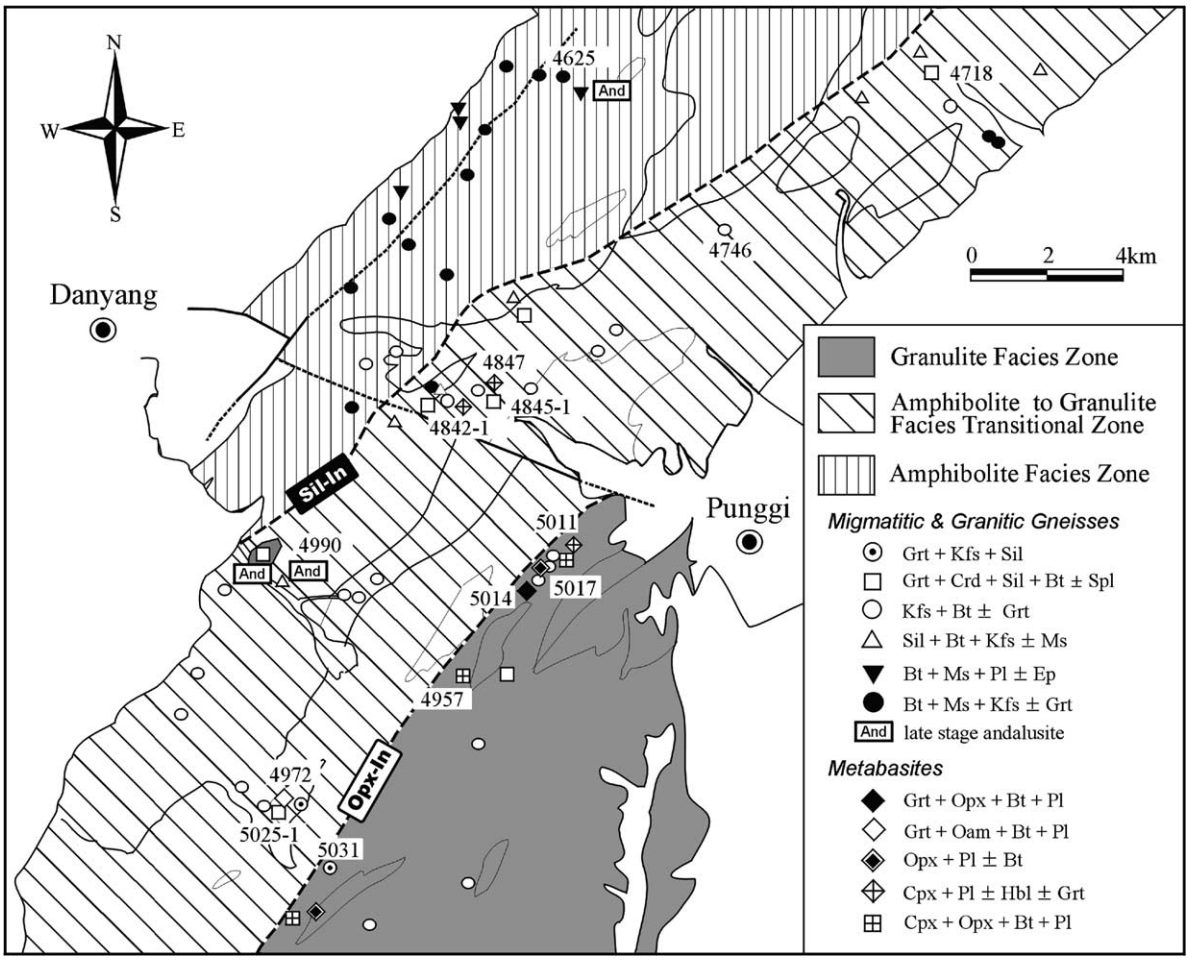

Fig. 2. Metamorphic-facies map of the study area. Mineral abbreviations are from Kretz (1983) and numbers are sample locations. Opx-In, orthopyroxene isograd in metabasites; Sil-In, sillimanite isograd in migmatitic and granitic gneisses.

diameter and contain plagioclase and biotite inclusions (Fig. 3B).

The biotite granitic gneiss is similar to the garnet granitic gneiss in texture and rock composition. This rock type is composed of biotite, muscovite, epidote, K-feldspar, plagioclase and quartz with or without minor garnet, fibrous sillimanite and andalusite.

Two different metabasites occur; one is rich in K, Na and Al (alkali metabasite), and the other is rich in Ca, Mg and Fe (calcic metabasite; Table 1). The alkali metabasite comprises orthoamphibole and/or orthopyroxene, clinopyroxene, plagioclase with minor garnet, biotite and quartz. On the other hand, the calcic metabasite comprises clinopyroxene, orthopyroxene, hornblende, plagioclase with minor biotite and quartz. The presence of orthopyroxene in metabasites is consistent with granulite-facies metamorphism. The rims of orthopyroxene grains are partly replaced by orthoamphibole (Fig. 3C). Thin coronas of secondary garnet occur between clinopyroxene and plagioclase in calcic metabasites (Fig. 3D).

In the study area, the metamorphic grade increases gradually towards southeast from the amphibolite to the granulite facies (Fig. 2). In the amphibolite-facies metamorphic zone, the biotite granitic gneiss displays

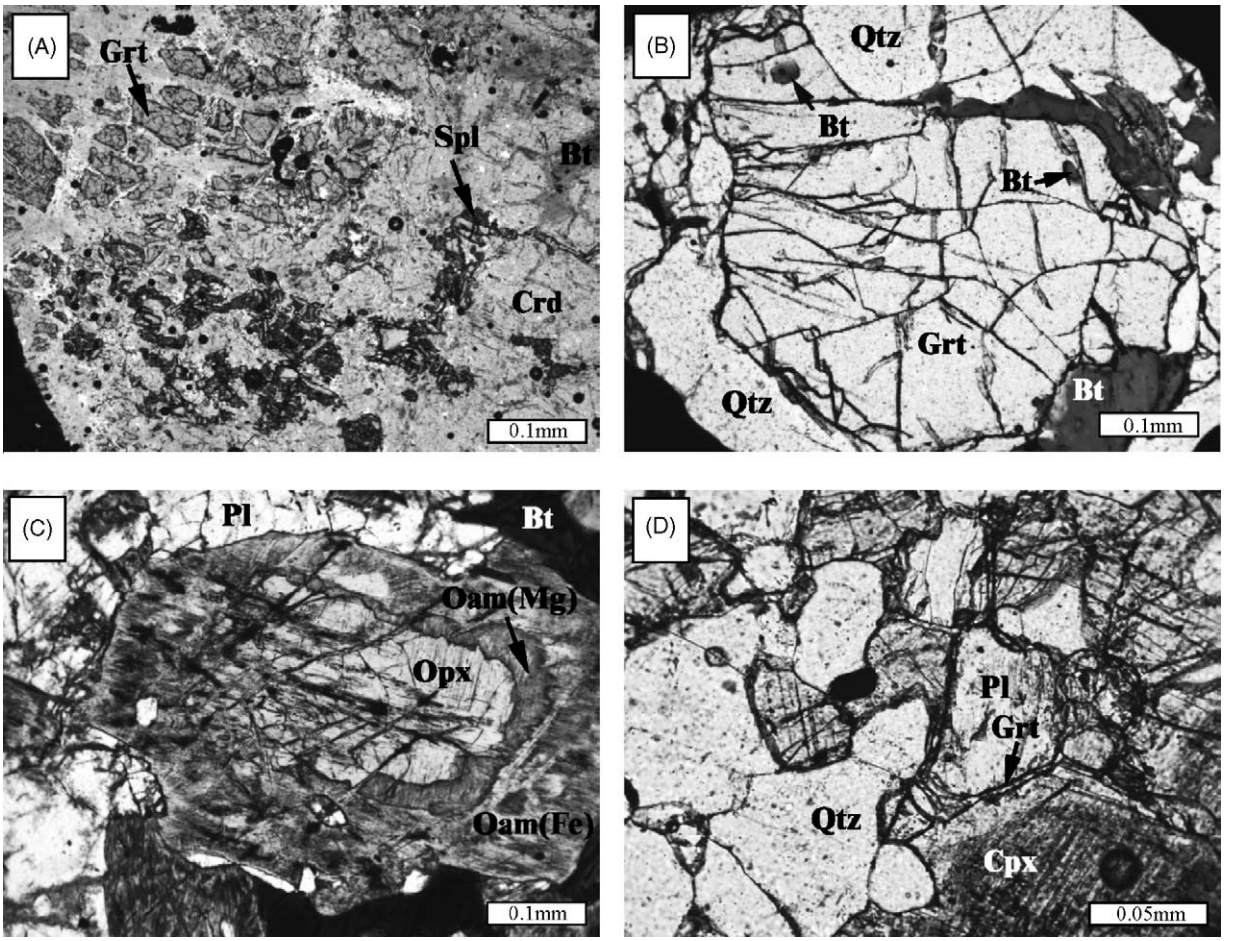

Fig. 3. (A) Corroded garnet and spinel enclosed in cordierite from migmatitic gneiss; (B) biotite inclusion within garnet porphyroblast in garnet granitic gneiss; (C) orthopyroxene rimmed by orthoamphibole in garnet-orthopyroxene metabasite; (D) coronitic secondary garnet between clinopyroxene and plagioclase in calcic metabasite. Mineral abbreviations are from Kretz (1983).

the mineral assemblage of biotite-muscovite-K-feldspar-plagioclase, with rare fine-grained and spessartine-rich garnet. In the amphibolite- to granulite-facies transitional zone, the amount and grain size of garnet increases, fibrous sillimanite appears at the expense of muscovite and, at the highest grade part of the transitional zone, fibrous sillimanite is gradually transformed to prismatic sillimanite. This observation indicates that the following reaction (1) occurred:

$$\underset{\text{muscovite}}{KAl_3Si_3O_{10}(OH)_2} + \underset{\text{quartz}}{SiO_2} = \underset{\text{K-feldspar}}{KAlSi_3O_8} + \underset{\text{parsillimanite}}{Al_2SiO_5} + \text{Melt} \quad (1)$$

In the transitional zone, garnet may also form by the reaction (2) in the sillimanite-bearing rocks:

$$\underset{\text{biotite}}{K(Mg, Fe)_3AlSi_3O_{10}(OH)_2} + \underset{\text{sillimanite}}{Al_2SiO_5} + \underset{\text{quartz}}{2SiO_2} = \underset{\text{garnet}}{(Mg, Fe)_3Al_2Si_3O_{12}} + \underset{\text{K-feldspar}}{KAlSi_3O_8} + \text{Melt} \quad (2)$$

The boundary for the granulite-facies zone is defined by the orthopyroxene-in (Opx-In) reaction. As metamorphic grade increases across this isograd, the mineral assemblage of calcic metabasites changes from clinopyroxene-amphibole-plagioclase-quartz to orthopyroxene-clinopyroxene-amphibole-plagioclase,

and that of alkali metabasites, from garnet-orthoamphibole-plagioclase to garnet-orthopyroxene-plagioclase. These changes are attributed to reactions (3) and (4):

$$\underset{\text{hornblende}}{Ca_2(Mg, Fe)_4Al_2Si_6O_{22}(OH)_2} + \underset{\text{quartz}}{SiO_2} = \underset{\text{orthopyroxene}}{3(Mg, Fe)SiO_3} + \underset{\text{clinopyroxene}}{Ca(Mg, Fe)Si_2O_6} + \underset{\text{anorthite}}{CaAl_2Si_2O_8} + H_2O \quad (3)$$

$$\underset{\text{cummingtonite}}{(Mg, Fe)_7Si_8O_{22}(OH)_2} = \underset{\text{orthopyroxene}}{7(Mg, Fe)SiO_3} + \underset{\text{quartz}}{SiO_2} + H_2O \quad (4)$$

A minor amount of hornblende is also found in alkali metabasites, indicating that reaction (5) may be also operative:

$$\underset{\text{tschermakite}}{Ca_2(Mg, Fe)_3Al_4Si_6O_{22}(OH)_2} + \underset{\text{quartz}}{3SiO_2} = \underset{\text{orthopyroxene}}{(Mg, Fe)SiO_3} + \underset{\text{garnet}}{Ca(Mg, Fe)_2Al_2Si_6O_{12}} + \underset{\text{anorthite}}{CaAl_2Si_2O_8} + H_2O \quad (5)$$

In the transitional- and granulite-facies zones, the garnet-cordierite-sillimanite-biotite-K-feldspar assemblage is observed in the Al_2O_3- and MgO-rich migmatitic gneiss and garnet granitic gneiss (Table 1). Cordierite grains contain inclusions of corroded garnet, sillimanite, spinel and quartz, suggesting that cordierite formed during retrograde metamorphism by reactions:

$$\underset{\text{garnet}}{(Mg, Fe)_3Al_2Si_3O_{12}} + \underset{\text{sillimanite}}{2Al_2SiO_5} = \underset{\text{spinel}}{3(Mg, Fe)Al_2O_4} + \underset{\text{quartz}}{5SiO_2} \quad (6)$$

and

$$\underset{\text{spinel}}{2(Mg, Fe)Al_2O_4} + \underset{\text{quartz}}{5SiO_2} = \underset{\text{cordierite}}{(Mg, Fe)_2Al_4Si_5O_{18}} \quad (7)$$

In the granulite-facies zone, reaction rims formed by the breakdown of orthopyroxene into orthamphibole during retrograde metamorphism probably occurred by reaction (8):

$$\underset{\text{orthopyroxene}}{7(Mg, Fe)SiO_3} + \underset{\text{quartz}}{SiO_2} + H_2O = \underset{\text{cummingtonite}}{(Mg, Fe)_7Si_8O_{22}(OH)_2} \quad (8)$$

Some orthoamphibole pseudomorphs have relics of garnet, orthopyroxene and quartz in sample 5014. In calcic metabasites 4842-1 and 5011, coronitic, fine-grained secondary garnet with quartz occur between clinopyroxene and plagioclase. This texture suggests that the new garnet formed during retrograde metamorphism by reaction (9):

$$\underset{\text{diopside/hedenbergite}}{Ca(Mg, Fe)Si_2O_6} + \underset{\text{anorthite}}{CaAl_2Si_2O_8} = \underset{\text{grossular}}{\tfrac{2}{3}Ca_3Al_2Si_3O_{12}} + \underset{\text{pyrope/almandine}}{\tfrac{1}{3}(Mg, Fe)_3Al_2Si_3O_{12}} + \underset{\text{quartz}}{SiO_2} \quad (9)$$

In some biotite granitic gneiss adjacent to the Mesozoic granite, andalusite formed during retrograde stage encloses and crosscuts high Ti biotite and muscovite.

3. Mineral chemistry

Mineral analyses were carried out on a JEOL JXA-8600SX electron microprobe at the Center for Mineral Resources Research, Korea University. Operating conditions were; acceleration voltage of 15 kV, beam current of 10 nA, and beam diameter of 5 μm. Total iron is considered as FeO. The mineral abbreviations of Kretz (1983) are used to describe the mineral assemblage and chemical reactions.

3.1. Plagioclase

The composition of plagioclase is presented in Table 2. Most of plagioclases grains do not show any chemical zoning. Plagioclase in migmatitic gneiss and biotite granitic gneiss is oligoclase ($An_{19–30}$). Plagioclase in the matrix of the garnet granitic gneiss has a lower An content ($An_{37–41}$) than plagioclase inclusions within garnet ($An_{45–46}$). Plagioclase in the garnet-orthopyroxene metabasite is andesine or labradorite ($An_{40–58}$) and that in garnet-orthoamphibole metabasite is andesine ($An_{47–48}$). Plagioclase

Table 2
Representative compositions of plagioclase

	Rock													
	Mig Gn			Grt Gr Gn			Bt Gr Gn		Mb-1		Mb-2		Mb-3	
	Sample			Sample			Sample		Sample		Sample		Sample	
	4845-1	4845-1	5025-1	5031	5031	5031[i]	4625	4625	5011	4847	5014	5014	4972	4972
SiO_2	63.50	60.54	60.74	58.58	58.73	56.63	61.19	62.87	44.17	47.31	57.92	53.77	56.32	55.93
TiO_2	0.01	0.00	0.01	0.01	0.09	0.00	0.00	0.00	0.00	0.00	0.07	0.21	0.00	0.05
Al_2O_3	22.76	24.29	24.07	26.27	25.74	27.19	24.01	23.30	34.51	33.21	26.45	29.50	27.40	27.36
FeO*	0.13	0.07	0.00	0.00	0.08	0.14	0.00	0.00	0.41	0.00	0.19	0.10	0.04	0.00
MnO	0.00	0.05	0.14	0.00	0.05	0.00	0.00	0.00	0.00	0.00	0.00	0.02	0.00	0.00
CaO	3.83	5.84	6.16	7.68	7.54	9.38	5.81	4.34	19.18	16.40	8.09	11.69	9.51	9.70
Na_2O	8.81	8.01	7.66	6.84	7.07	6.22	7.88	8.66	0.84	1.97	6.63	4.83	5.95	5.87
K_2O	0.13	0.20	0.45	0.18	0.09	0.08	0.00	0.00	0.00	0.04	0.27	0.09	0.03	0.04
Total	99.17	99.00	99.23	99.56	99.39	99.64	98.89	99.17	99.11	98.93	99.62	100.21	99.25	98.95
Cations per 8 oxygens														
Si	2.821	2.717	2.722	2.624	2.636	2.551	2.739	2.794	2.066	2.190	2.601	2.425	2.544	2.536
Al	1.191	1.284	1.271	1.386	1.361	1.442	1.266	1.220	1.901	1.810	1.399	1.567	1.458	1.461
Ti	0.000	0.000	0.000	0.000	0.003	0.000	0.000	0.000	0.000	0.000	0.002	0.007	0.000	0.002
Fe^{2+}	0.005	0.003	0.000	0.000	0.003	0.005	0.000	0.000	0.016	0.000	0.007	0.004	0.002	0.000
Mn	0.000	0.002	0.005	0.000	0.002	0.000	0.000	0.000	0.000	0.000	0.000	0.001	0.000	0.000
Ca	0.182	0.281	0.296	0.369	0.363	0.453	0.279	0.207	0.961	0.813	0.389	0.565	0.460	0.471
Na	0.759	0.697	0.666	0.594	0.615	0.543	0.684	0.746	0.076	0.177	0.577	0.422	0.521	0.516
K	0.007	0.011	0.026	0.010	0.005	0.005	0.000	0.000	0.000	0.002	0.015	0.005	0.002	0.002
Total cation	4.965	4.995	4.986	4.983	4.988	4.999	4.968	4.967	5.020	4.992	4.990	4.996	4.987	4.988
X_{Ab}	0.80	0.71	0.67	0.61	0.63	0.54	0.71	0.78	0.07	0.18	0.59	0.43	0.53	0.52
X_{An}	0.19	0.28	0.30	0.38	0.37	0.45	0.29	0.22	0.93	0.82	0.40	0.57	0.47	0.48
X_{Or}	0.01	0.01	0.03	0.01	0.01	0.01	0.00	0.00	0.00	0.00	0.02	0.01	0.00	0.00

Abbreviations are same as Table 1 and Mb-3 is alkali metabasite containing orthoamphibole. FeO*, total iron as FeO; *i*, inclusion; $X_{Ab} = Na/(Na + Ca + K)$, $X_{An} = Ca/(Na + Ca + K)$, $X_{Or} = K/(Na + Ca + K)$.

in the calcic metabasite is bytownite-anorthite ($An_{82–98}$).

3.2. Biotite

The composition of biotite is presented in Table 3 and Fig. 4. The X_{Fe} of biotite in migmatitic gneiss has a wide compositional range from 0.34 to 0.78. In contrast, the X_{Fe} of biotite in other rock types have narrow ranges of 0.41–0.55 (garnet granitic gneiss), 0.34–0.51 (garnet-orthopyroxene metabasite) and 0.47–0.53 (garnet-orthoamphibole metabasite), respectively. In the migmatitic gneiss, garnet granitic gneiss, and garnet-orthopyroxene metabasite, Ti and Al^{VI} of biotite inclusions in garnet and matrix biotite are higher than that of biotite in contact with garnet rims. The Al^{IV} of biotite in all rock types is 1.20–1.39 a.p.f.u.

3.3. Garnet

The composition of garnet is presented in Table 4 and Fig. 5. The garnet grains have almost homogeneous compositions except for rims, and their representative compositions in migmatitic gneiss and garnet granitic gneiss are $Alm_{72–78}Prp_{18–25}Sps_{0–4}Grs_{2–4}$ and $Alm_{66–68}Prp_{25–27}Sps_{1–4}Grs_{3–5}$, respectively. On the other hand, garnet in the biotite granitic gneiss is relatively spessatine rich ($Alm_{65–74}Prp_{6–9}Sps_{14–26}Grs_{2–3}$) and that in calcic metabasite is grossular rich ($Alm_{56–66}Prp_{4–13}Sps_{3–14}Grs_{19–27}$). Garnet in the garnet-orthopyroxene metabasite is higher in the pyrope content ($Alm_{66–67}Prp_{26–27}Sps_{1–3}Grs_{5–7}$) than that in garnet-orthoamphibole metabasite ($Alm_{69–74}Prp_{16–22}Sps_4Grs_6$). In the garnet-orthopyroxene metabasite, the compositions of rims are different

Table 3
Representative compositions of biotite

	Rock														
	Mig Gn					Grt Gr Gn				Bt Gr Gn	Mb-2				Mb-3
	Sample					Sample				Sample	Sample				Sample
	4718^{i}	4746^{r}	$4845\text{-}1^{m}$	$5025\text{-}2^{m}$	4990^{m}	5031^{i}	5031^{m}	5031^{r}	5031^{r}	4625^{r}	5014^{i}	5014^{m}	5014^{r}	5014^{r}	4972^{I}
SiO_2	36.30	35.37	34.56	33.79	33.40	35.37	34.94	34.86	35.21	34.64	35.65	34.99	35.85	35.28	35.87
TiO_2	3.71	1.86	2.52	3.23	3.43	2.03	2.21	1.26	0.58	0.90	3.41	5.36	1.69	0.58	1.94
Al_2O_3	17.59	18.29	17.84	18.78	18.51	17.39	17.61	18.04	18.43	18.72	16.00	15.01	16.42	17.26	16.79
FeO	14.62	20.88	20.28	22.40	24.47	20.67	19.15	19.99	19.24	21.94	18.93	19.98	18.73	19.80	18.31
MnO	0.00	0.00	0.08	0.13	0.00	0.09	0.03	0.00	0.00	0.53	0.00	0.00	0.00	0.12	0.00
MgO	13.07	8.42	8.29	6.20	4.71	9.57	10.22	9.87	10.40	7.98	11.35	10.76	11.83	11.53	11.40
CaO	0.00	0.00	0.05	0.00	0.09	0.00	0.00	0.03	0.00	0.00	0.00	0.00	0.03	0.00	0.08
Na_2O	0.46	0.37	0.42	0.44	0.41	0.57	0.49	0.55	0.59	0.29	0.44	0.42	0.35	0.41	0.52
K_2O	9.63	9.66	9.80	9.68	9.95	10.20	9.77	10.11	10.09	9.19	8.98	8.82	9.32	9.41	9.80
Total	95.38	94.85	93.84	94.65	94.97	95.89	94.42	94.71	94.54	94.19	94.76	95.34	94.22	94.39	94.76
Cations per 11 oxygens															
Si	2.706	2.732	2.699	2.646	2.639	2.717	2.701	2.701	2.719	2.711	2.730	2.685	2.757	2.728	2.749
Al(IV)	1.294	1.268	1.301	1.354	1.361	1.283	1.299	1.299	1.281	1.289	1.270	1.315	1.243	1.272	1.251
Al(VI)	0.250	0.396	0.340	0.378	0.361	0.291	0.305	0.349	0.395	0.436	0.173	0.041	0.244	0.300	0.264
Ti	0.208	0.108	0.148	0.190	0.204	0.117	0.128	0.073	0.034	0.053	0.196	0.309	0.098	0.034	0.112
Fe^{2+}	0.911	1.349	1.325	1.467	1.617	1.327	1.238	1.295	1.242	1.436	1.212	1.282	1.204	1.281	1.173
Mn	0.000	0.000	0.005	0.009	0.000	0.006	0.002	0.000	0.000	0.035	0.000	0.000	0.000	0.008	0.000
Mg	1.452	0.970	0.965	0.724	0.555	1.096	1.178	1.140	1.197	0.931	1.296	1.231	1.356	1.329	1.302
Ca	0.000	0.000	0.004	0.000	0.008	0.000	0.000	0.002	0.000	0.000	0.000	0.000	0.002	0.000	0.007
Na	0.066	0.055	0.064	0.067	0.063	0.085	0.073	0.083	0.088	0.044	0.065	0.062	0.052	0.061	0.077
K	0.916	0.952	0.976	0.967	1.003	0.999	0.963	0.999	0.994	0.917	0.877	0.863	0.914	0.928	0.958
Total cation	7.803	7.830	7.827	7.802	7.811	7.921	7.887	7.941	7.950	7.852	7.819	7.788	7.870	7.941	7.893
X_{fe}	0.39	0.58	0.58	0.67	0.74	0.55	0.51	0.53	0.51	0.61	0.48	0.51	0.47	0.49	0.47

Abbreviations are same as Tables 1 and 2. *i*, inclusion in garnet or orthopyroxene; *r*, in contact with garnet; *m*, matrix; $X_{Fe} = Fe^{2+}/(Fe^{2+} + Mg)$.

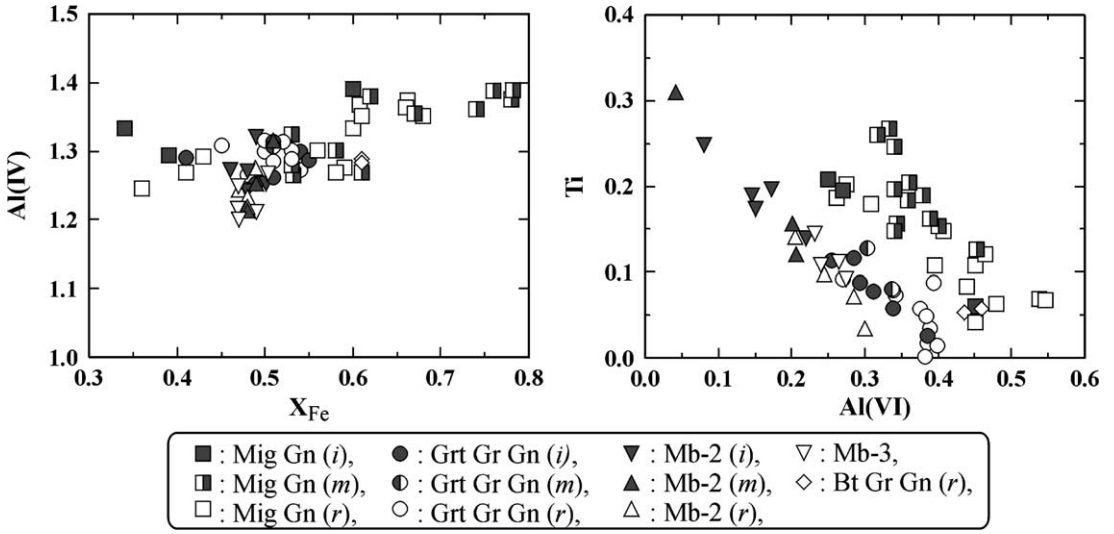

Fig. 4. Biotite compositions plotted in X_{Fe} vs. Al(IV) and Al(VI) vs. Ti diagrams. The compositional range of biotite is slightly different according to the whole rock chemistry. Rock abbreviations are same as in Tables 1 and 2. *i*, inclusion in garnet or orthopyroxene; *r*, in contact with garnet; *m*, matrix.

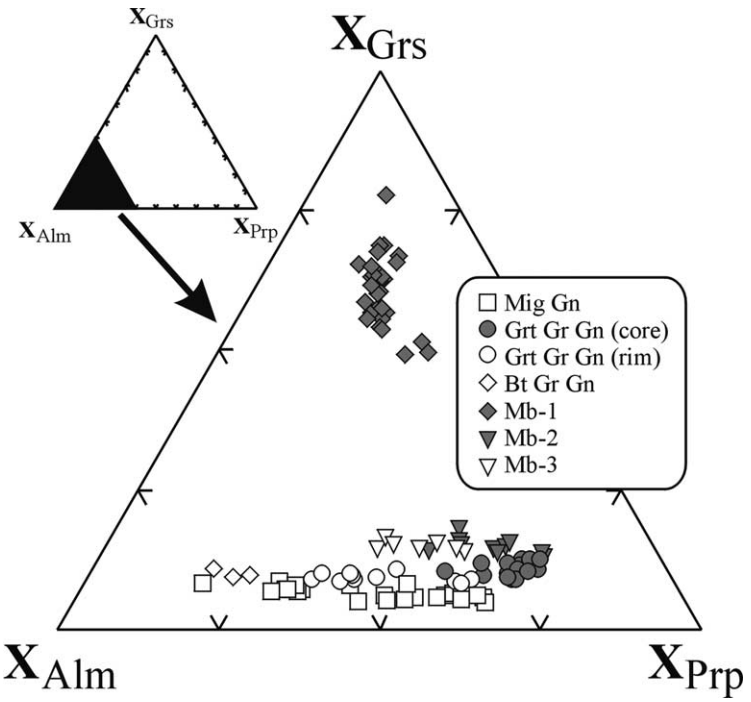

Fig. 5. Compositional variation of garnet. Rock abbreviations are same as in Tables 1 and 2.

Table 4
Representative compositions of garnet

	Rock															
	Mig Gn					Grt Gr Gn			Bt Gr Gn		Mb-1		Mb-2		Mb-3	
	Sample					Sample			Sample		Sample		Sample		Sample	
	4845-1^r	4845-1^r	5025-1^r	5025-1^r	4718^r	5031^c	5031^r	5031^r	4625^r	4625^r	5011^r	4842-1^r	5014^c	5014^r	4972^r	4972^r
SiO_2	37.90	37.35	36.64	36.38	37.19	38.03	36.97	37.36	36.29	36.42	37.01	36.62	37.89	38.14	37.29	37.33
Al_2O_3	21.41	21.23	20.79	20.67	21.02	21.20	21.32	21.39	20.98	20.54	20.53	20.44	21.45	21.32	20.79	21.37
FeO	32.28	33.61	35.78	36.06	34.61	31.13	33.81	35.54	32.99	28.67	28.44	26.86	30.45	31.00	33.13	30.79
MnO	0.18	0.36	1.18	2.96	0.58	0.68	1.43	1.15	6.25	11.37	4.44	5.91	0.90	0.58	1.79	1.77
MgO	6.37	5.91	3.18	1.67	4.75	6.46	3.90	3.89	2.16	1.40	2.14	1.66	7.00	6.14	4.10	5.38
CaO	0.77	0.93	1.04	1.00	0.73	1.39	1.29	1.17	1.15	1.09	6.99	7.78	1.86	1.91	1.99	1.93
Na_2O	0.38	0.33	0.41	0.30	0.26	0.27	0.27	0.33	0.00	0.25	0.00	0.34	0.47	0.40	0.34	0.19
Total	99.29	99.72	99.02	99.04	99.14	99.16	98.99	100.83	99.82	99.74	99.55	99.61	100.02	99.48	99.43	98.76
Cations per 12 oxygens																
Si	2.993	2.951	2.966	2.979	2.983	3.003	2.986	2.974	2.952	2.974	2.978	2.940	2.951	3.011	2.986	2.980
Al	1.990	1.975	1.981	1.994	1.985	1.972	2.029	2.007	2.011	1.976	1.946	1.933	1.967	1.982	1.960	2.009
Fe^{2+}	2.132	2.221	2.422	2.470	2.321	2.056	2.284	2.366	2.245	1.958	1.914	1.804	1.983	2.047	2.218	2.055
Mg	0.750	0.696	0.384	0.204	0.568	0.761	0.470	0.462	0.262	0.170	0.257	0.199	0.813	0.722	0.489	0.640
Mn	0.012	0.024	0.081	0.205	0.039	0.045	0.098	0.077	0.431	0.787	0.303	0.402	0.059	0.039	0.121	0.120
Ca	0.065	0.079	0.090	0.088	0.063	0.118	0.112	0.100	0.100	0.095	0.603	0.669	0.155	0.161	0.171	0.165
Na	0.058	0.051	0.064	0.048	0.040	0.041	0.042	0.051	0.000	0.040	0.000	0.053	0.071	0.062	0.053	0.029
Total cation	8.000	7.997	7.988	7.988	7.999	7.996	8.021	8.037	8.001	8.000	8.001	8.000	7.999	8.024	7.998	7.998
X_{alm}	0.72	0.74	0.81	0.83	0.78	0.69	0.77	0.79	0.74	0.65	0.62	0.59	0.66	0.69	0.74	0.69
X_{Prp}	0.25	0.23	0.13	0.07	0.19	0.26	0.16	0.15	0.09	0.06	0.08	0.07	0.27	0.24	0.16	0.22
X_{Grs}	0.02	0.03	0.03	0.03	0.02	0.04	0.04	0.03	0.03	0.03	0.20	0.22	0.05	0.05	0.06	0.06
X_{Sps}	0.00	0.01	0.03	0.07	0.01	0.02	0.03	0.03	0.14	0.26	0.10	0.13	0.02	0.01	0.04	0.04
X_{fe}	0.74	0.76	0.86	0.92	0.80	0.73	0.83	0.84	0.90	0.92	0.88	0.90	0.71	0.74	0.82	0.76

Abbreviations are same as Tables 1 and 2. *c*, core; *r*, rim; X_{Alm}, Fe^{2+}/M; X_{Prp}, Mg/M; X_{Grs}, Ca/M; X_{Sps}, Mn/M where $M = Fe^{2+} + Mg + Ca + Mn$; $X_{Fe} = Fe^{2+}/(Fe^{2+} + Mg)$.

depending upon the adjacent mineral. The rim part in contact with plagioclase show little compositional variation but that in contact with biotite has higher X_{Alm} and lower X_{Prp} than the inner part (Fig. 6A). Similar relationship is also found in the garnet granitic gneiss and the migmatitic gneiss (Fig. 6B and C). Tracy (1982) suggested that the compositional pattern could be attributed to Fe–Mg exchange between garnet and adjacent ferromagnesian minerals, and diffusion on grain boundary during retrogression.

4. Pyroxene, amphibole and other minerals

Orthopyroxene has X_{Fe} and Al contents of 0.49–0.51 and 0.12 a.p.f.u., respectively, and does not shows a significant chemical zoning (Table 5, Fig. 7). In contrast, the X_{Fe} of orthoamphibole rimming orthopyroxene increases from 0.22 to 0.49 away from the orthopyroxene. The X_{Fe} and Al contents of clinopyroxene in metabasites are 0.39–0.61 and 0.01–0.06 a.p.f.u., respectively. Amphibole in metabasite

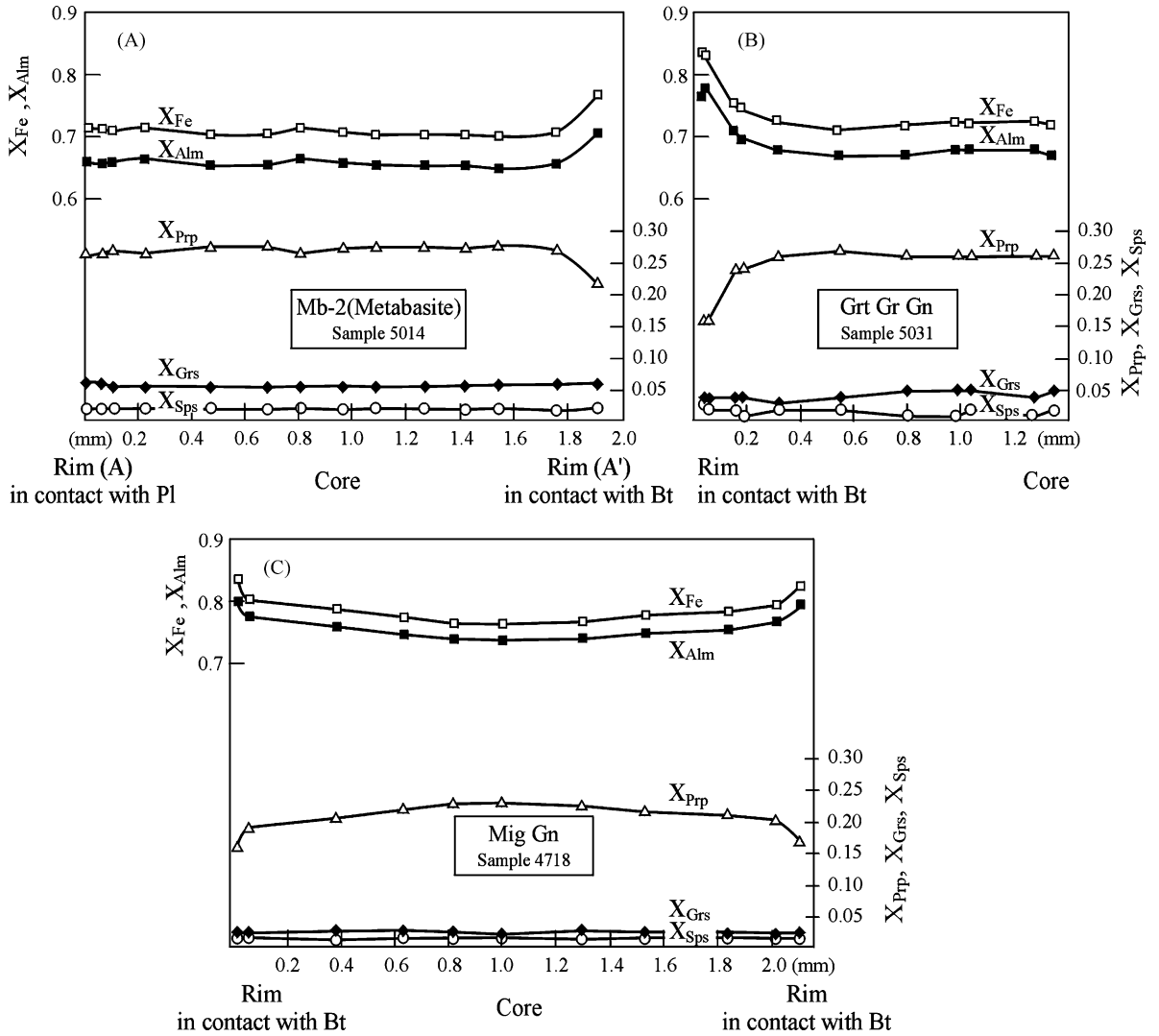

Fig. 6. Compositional profiles of garnets in the garnet-orthopyroxene metabasite (A), garnet granitic gneiss (B), and migmatitic gneiss (C).

Table 5
Representative compositions of pyroxene, amphibole, cordierite and spinel

	Rock															
	Mb-1			Mb-2		Mb-1			Mb-2		Mig Gn					
	Sample			Sample		Sample			Sample		Sample					
	5011	4847	4842-1	5014	5014	4842-1	4847	4847	5014	5014	4845-1	5025-2	4845-1	4845-1	4845-1	4990
	Mineral			Mineral		Mineral			Mineral		Mineral					
	Cpx	Cpx	Cpx	Opx	Opx	Fe-Hb	Mg-Hb	Act	Cum	Cum	Crd	Crd	Spl	Spl	Sil	And
SiO_2	50.97	52.09	50.62	49.83	49.75	43.08	48.27	54.07	58.13	52.87	48.31	46.86	0.00	0.00	35.96	36.11
TiO_2	0.00	0.19	0.00	0.02	0.06	0.46	1.12	0.11	0.00	0.00	0.16	0.05	0.00	0.07	0.04	0.00
Al_2O_3	0.95	0.91	0.99	2.75	2.72	12.15	7.17	1.07	2.74	0.68	33.07	32.62	56.78	55.57	62.69	63.12
FeO	16.55	12.35	17.50	29.39	30.24	22.14	15.63	16.8	11.97	26.88	6.36	10.35	34.07	35.96	0.48	0.26
MnO	0.87	0.19	0.92	0.09	0.34	0.65	0.00	0.00	0.00	0.36	0.00	0.24	0.23	0.00	0.02	0.00
MgO	9.11	11.34	8.33	16.61	16.55	6.09	12.4	13.17	22.12	15.44	9.03	6.62	2.35	2.29	0.00	0.00
CaO	20.96	22.38	21.04	0.29	0.20	11.3	11.76	11.9	0.1	0.33	0.02	0.08	0.04	0.00	0.06	0.00
Na_2O	0.33	0.27	0.24	0.43	0.52	1.14	0.87	0.23	0.57	0.4	0.10	0.39	2.15	1.91	0.00	0.00
Total	99.74	99.72	99.64	99.41	100.38	97.01	97.22	97.35	95.63	96.96	97.05	97.21	95.62	95.80	99.25	99.49
	O=6					O=23					Cat = 11		O = 4		O = 5	
Si	1.973	1.980	1.973	1.918	1.904	6.609	7.103	7.913	8.106	7.920	5.006	4.954	0.000	0.000	0.981	0.981
Al	0.043	0.041	0.045	0.125	0.122	2.195	1.243	0.185	0.450	0.120	4.036	4.062	1.982	1.928	2.014	2.019
Ti	0.000	0.005	0.000	0.001	0.002	0.053	0.124	0.012	0.000	0.000	0.012	0.004	0.000	0.002	0.004	0.000
Fe^{2+}	0.535	0.392	0.571	0.946	0.968	2.840	1.920	2.060	1.400	3.370	0.551	0.915	0.845	0.886	0.011	0.006
Mn	0.029	0.006	0.030	0.003	0.011	0.084	0.000	0.000	0.000	0.046	0.000	0.021	0.000	0.000	0.000	0.000
Mg	0.526	0.643	0.484	0.953	0.944	1.390	2.720	2.870	4.600	3.450	1.395	1.043	0.104	0.101	0.000	0.000
Ca	0.869	0.912	0.879	0.012	0.008	1.860	1.850	1.870	0.020	0.050	0.002	0.009	0.000	0.000	0.002	0.000
Na	0.025	0.020	0.018	0.032	0.039	0.340	0.250	0.070	0.150	0.120	0.020	0.080	0.124	0.109	0.000	0.001
Total cation	4.000	3.999	4.000	3.990	3.998	15.371	15.210	14.980	14.726	15.076	11.022	11.088	3.055	3.025	3.012	3.007
Wo	0.44	0.47	0.45	0.01	0.00											
En	0.27	0.33	0.25	0.50	0.49											
Fs	0.29	0.20	0.31	0.50	0.51											

Abbreviations are same as Tables 1 and 2. Wo, $Ca/(Ca + Fe^{2+} + Mg)$; En, $Mg/(Ca + Fe^{2+} + Mg)$; Fs, $Fe^{2+}/(Ca + Fe^{2+} + Mg)$.

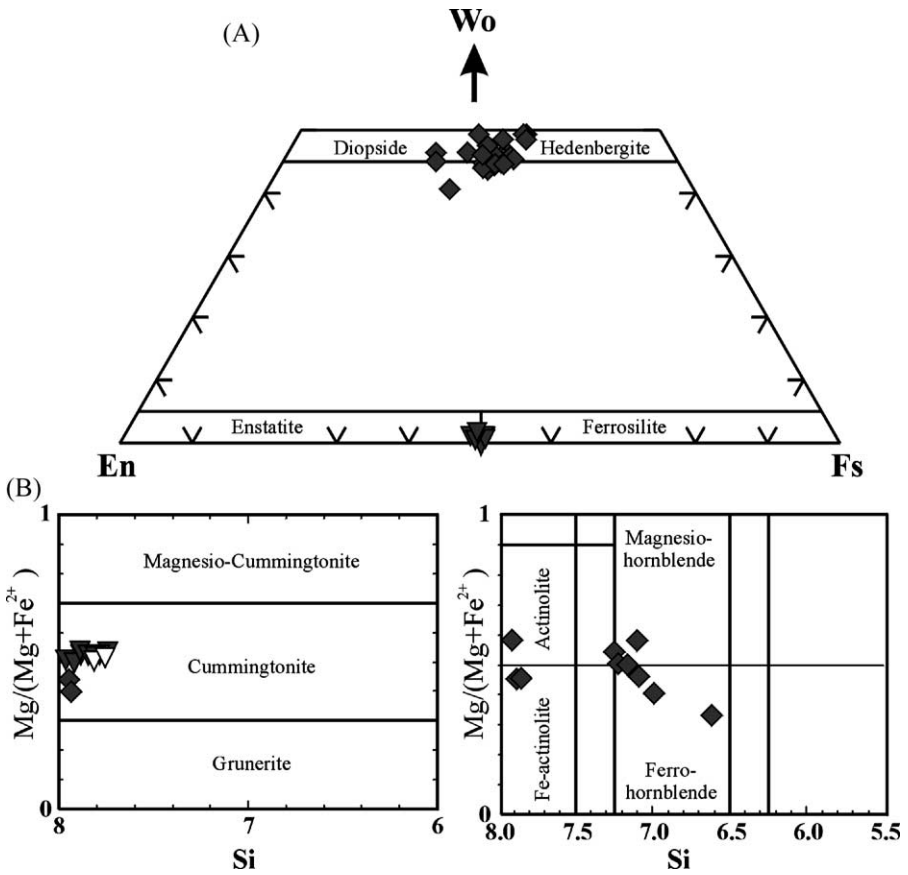

Fig. 7. Classification and compositional variation of (A) pyroxene and (B) amphibole in metabasites. Symbols in Fig. 4 are used.

is mostly magnesio- to ferro-hornblende but, locally, actinolite occurs as a retrogressive product.

Cordierite is Mg-rich, with X_{Fe} ranging from 0.28 to 0.47. Spinel in cordierite is Fe-rich with X_{Fe} ranging from 0.76 to 0.90 (Table 5). The Si and Al contents of aluminosilicates (sillimanite and andalusite) are 0.981 and 2.014–2.019 a.p.f.u., respectively.

5. Metamorphic condition

To determine the metamorphic conditions, the TWEEQU program (Berman, 1991) and the following conventional geothermobarometers were used: garnet-orthopyroxene geothermometer of Harley (1984), garnet-orthopyroxene-plagioclase-quartz geobarometer of Eckert et al. (1991), garnet-biotite geothermometer of Perchuk and Lavrent'eva (1983), garnet-biotite-plagioclase geobarometer of Hoisch (1990) and GASP geobarometer of Koziol and Newton (1988).

The rims of orthopyroxene grains in the granulite-facies garnet-orthopyroxene metabasite were transformed to orthoamphibole during retrograde metamorphism, with the result that orthopyroxene and garnet are no longer in direct contact. As discussed in Section 3, the outer rim of garnet had undergone a compositional change during retrograde metamorphism but the cores of garnet and orthopyroxene were not affected by it. Under the assumption that garnet core and orthopyroxene core were at equilibrium with plagioclase in the matrix during the peak metamorphism, the peak *P–T* conditions calculated using core pairs are 800–815 °C and 6.1–8.4 kb (Fig. 8, Table 6). The *P–T* conditions calculated from garnet core together with biotite and plagioclase in the matrix from

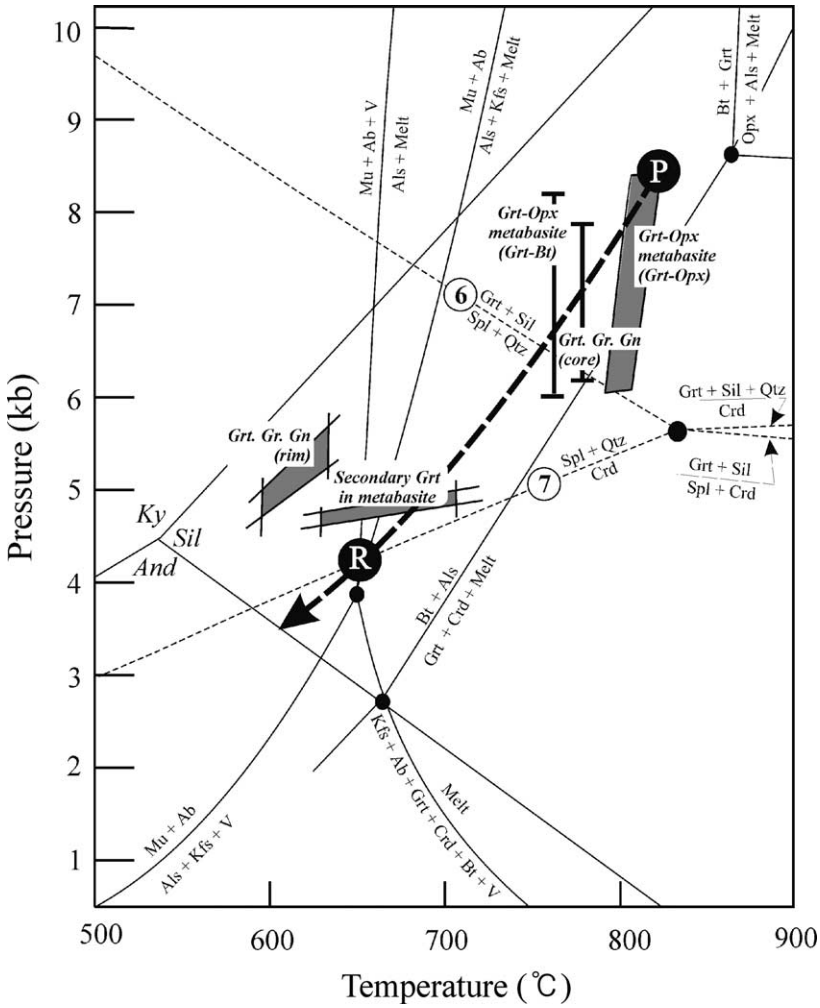

Fig. 8. *P–T* conditions and the inferred *P–T* path (dashed arrow). Phase equilibria involving cordierite and spinel (dashed lines) in the migmatitic gneiss (sample 4845-1) is calculated in KMASH system using the TWEEQU program (Berman, 1991). Petrogenetic grid for the NaKFMASH system (solid curve) is from Spear et al. (1999). P and R are the *P–T* conditions of peak and retrograde metamorphic stage, respectively.

the same sample are 767 °C and 6.0–8.2 kb. Thus, peak *P–T* conditions of garnet-orthopyroxene metabasites are 767–815 °C and 6.0–8.4 kb. On the other hand, their retrograde *P–T* conditions calculated using garnet rim and adjacent biotite and plagioclase are 677 °C and 4.8–6.4 kb.

In the garnet granitic gneiss 5031 in the granulite-facies zone, the peak metamorphic condition was estimated on the assumption that plagioclase and biotite in matrix, far apart from garnet, were stable with garnet cores. The result suggests a *P–T* condition of 772 °C and 6.2–7.9 kb. The retrograde *P–T* conditions calculated from garnet rims and adjacent biotite, plagioclase and sillimanite are 595–626 °C, 4.7–5.7 kb. The *P–T* condition calculated from secondary garnet in the mafic granulite 5011 is 707 °C and 4.9 kb using the TWEEQU program (Berman, 1991).

The *P–T* estimations from the granulite-facies zone are summarized in Fig. 8 and indicate that (1) both garnet-orthopyroxene metabasite and garnet granitic gneiss had undergone upper amphibolite-facies retrograde metamorphism following granulite-facies

Table 6
Pressure and temperature conditions estimated from various metamorphic rocks

	Grt Gr Gn			Mb-2			Mb-2		Mb-1	
	5031			5014			5014		5011	4842-1
Grt	*c*	*r*	*r*	*c*	*r*	Grt	*c*	Grt	*r*	*r*
X_{alm}	0.67	0.77	0.78	0.65	0.71	X_{Alm}	0.66	X_{alm}	0.62	0.56
X_{Prp}	0.26	0.16	0.14	0.27	0.22	X_{Prp}	0.27	X_{Prp}	0.08	0.04
X_{Grs}	0.05	0.04	0.04	0.05	0.06	X_{Grs}	0.05	X_{Grs}	0.20	0.27
X_{Sps}	0.02	0.03	0.04	0.02	0.02	X_{Sps}	0.02	X_{Sps}	0.10	0.13
Bt	*m*	*r*	*r*	*m*	*r*	Opx	*c*	Cpx	*r*	*r*
X_{fe}	0.43	0.45	0.43	0.43	0.42	X_{Fs}	0.50	X_{Fs}	0.29	0.26
X_{ti}	0.05	0.03	0.01	0.05	0.04	X_{En}	0.49	X_{en}	0.27	0.25
$X_{Al(VI)}$	0.11	0.12	0.14	0.07	0.09	X_{Wo}	0.01	X_{Wo}	0.44	0.48
Pl	*m*	*m*	*m*	*m*	*m*		*m*		*r*	*r*
X_{An}	0.37–0.41	0.37–0.41	0.37–0.41	0.40–0.57	0.40–0.57	X_{An}	0.40–0.57	X_{An}	0.93	0.97
T^{PL} (°C)	772	626	595	767	677	T^{ha} (°C)	800–815	T^{TWQ} (°C)	707	635
P^{KN} (kb)		5.3–5.7	4.7–5.0			P^{ec} (kb)	6.1–8.4	P^{TWQ} (kb)	4.9	4.7
P^{Ho} (kb)	6.2–7.9			6.0–8.2	4.8–6.4					

Abbreviations are same as Tables 1 and 2. PL, Perchuk and Lavrent'eva (1983); KN, Koziol and Newton (1988); Ho, Hoisch (1990); Ha, Harley (1984); Ec, Eckert et al. (1991); TWQ, Berman (1991).

metamorphism, (2) the peak metamorphic conditions are 767–815 °C and 6.0–8.4 kb, and (3) the *P–T* conditions of retrograde metamorphism are 595–707 °C and 4.7–6.4 kb.

The *P–T* condition in the transition zone, calculated from secondary garnet of metabasites (4842-1) is 635 °C and 4.7 kb using the TWEEQU program (Berman, 1991). In order to constrain the stability fields of cordierite and spinel from cordierite-bearing migmatitic gneiss (4845-1) in the transition zone, phase equilibria in the K_2O–MgO–Al_2O_3–SiO_2–H_2O (KMASH) system were calculated using the TWEEQU (Berman, 1991) (Fig. 8). The activities of pyrope, phlogopite, cordierite and spinel were calculated using ideal site mixing models of Berman and Aranovich (1996). As described earlier, the retrogression of the migmatitic gneiss is represented by reactions (6) and (7). Their *P–T* conditions are compatible with those estimated from the metabasite, suggesting that the retrograde *P–T* path in the transition zone is similar to that in the granulite-facies zone.

6. Age determination

To determine the ages of intrusion and metamorphism of garnet granitic gneiss, U–Pb zircon and Sm–Nd whole rock-garnet isochron age-datings were carried out for a granulite-facies zone sample 5017 (Fig. 2). After crushing, a Wilfley table was used to concentrate heavy minerals. Heavy minerals were separated first by magnetic separation using a Frantz magnetic separator, and then by heavy liquid separation using sodium polytungstate with distilled water. Finally zircon and garnet fractions were hand-picked under a binocular microscope.

6.1. U–Pb zircon ages

Most of zircon grains separated from garnet granitic gneiss are euhedral to subhedral, brown and transparent. Zircons are classified into three types: (1) long prismatic zircon with length longer than 250 μm and aspect ratio higher than 1:3 (Type I); (2) medium-sized tabular zircon 150–250 μm in length and with aspect ratios of 1:2–1:3 (Type II); and (3) small and round zircon shorter than 150 μm in length and with aspect ratios of 1:1–1:1.5 (Type III). Single grains of each type were analyzed (Table 7). Zircon was dissolved with mixed HF–HNO_3 solution. A mixed ^{235}U–^{205}Pb spike was used. U and Pb extraction procedure was standard ion exchange column method. Isotopic analyses were performed on a VG354 thermal ionization mass spectrometer using a Daly detector at the Tianjin

Table 7
U and Pb abundances, isotope ratios and ages of zircon in garnet granitic gneiss

Sample	Shape[a]	U (ppm)	Pb (ppm)	$^{206}Pb/^{204}Pb$	$^{208}Pb/^{206}Pb$	$^{206}Pb/^{238}U$	$^{207}Pb/^{235}U$	$^{207}Pb/^{206}Pb$	$^{206}Pb/^{238}U$ (Ma)	$^{207}Pb/^{235}U$ (Ma)	$^{207}Pb/^{206}Pb$ (Ma)
5017-zr-1	Type II	1057	353	20,271	0.05330	0.3313 ± 0.0010	5.308 ± 0.0017	0.1162 ± 0.0001	1845	1870	1899
5017-zr-2	Type I	1559	499	29,082	0.04517	0.3196 ± 0.0005	5.122 ± 0.0008	0.1162 ± 0.0001	1788	1840	1899
5017-zr-3	Type II	633	200	9,905	0.07755	0.3056 ± 0.0016	4.889 ± 0.0028	0.1160 ± 0.0003	1719	1800	1896
5017-zr-4	Type III	853	229	9,571	0.04726	0.2671 ± 0.0008	4.235 ± 0.0016	0.1150 ± 0.0002	1526	1681	1880

[a] Detail descriptions on the shape are given in text.

Table 8
Sm and Nd abundances and isotope ratios of whole rock and garnet in garnet granitic gneiss

Sample	Sm (ppm)	Nd (ppm)	$^{147}Sm/^{144}Nd$	$^{143}Nd/^{144}Nd$	2s	T_{DM}
5017 wr	7.487	43.597	0.1039	0.511225	0.000016	2.53
5017 grt-1	4.376	2.687	0.9851	0.514740	0.000060	
5017 grt-2	4.255	2.332	1.1036	0.515269	0.000019	

Institute of Geology and Mineral Resources. U and Pb were loaded onto Re filaments in silica gel–phosphoric acid mixture. U and Pb were analyzed at temperatures, between 1450 and 1500 °C and between 1300 and 1450 °C, respectively. All zircon analyses were corrected for 20–30 pg of total laboratory Pb blank and 2–6 pg of total laboratory U blank. The decay constants used in calculations are 9.8485×10^{-10} per year for ^{235}U and 1.5513×10^{-10} per year for ^{238}U (Steiger and Jäger, 1977). The data reduction and statistical evaluation are done using the ISOPLOT program (ver. 2.71) of Ludwig (1994). Error ellipses on concordia diagram and errors on zircon ages are given at the 2σ (95% confidence limit) level. Because small amounts of sample were used, uncertainties in U and Pb concentration may be as high as 20%.

Analyzed data were plotted on the concordia diagram (Table 8, Fig. 9). The analyzed data are discordant but collinear within experimental error. The upper intercept age is 1904 ± 9 Ma with mean square of weighted deviates (MSWD) of 6.7, which is inferred as an intrusion age of garnet granitic gneiss. This age is very common in the Yeongnam Massif. Turek and Kim (1996) reported a conventional U–Pb zircon age of 1945 ± 5 Ma from porphyroblastic gneiss and 1923 ± 23 Ma from granitic gneiss at the southwestern part of the Massif, whereas Park et al. (1993) reported Pb–Pb whole rocks age of 1920 ± 56 Ma from granitic gneiss at the northeastern part of the Massif. Thus, it appears that the Yeongnam Massif was affected by major magmatic activity at ca. 1.9 Ga.

6.2. Sm–Nd whole rock-garnet isochron age

About 100 mg of rock powder and garnet fractions, respectively were mixed with a ^{150}Nd–^{149}Sm spike

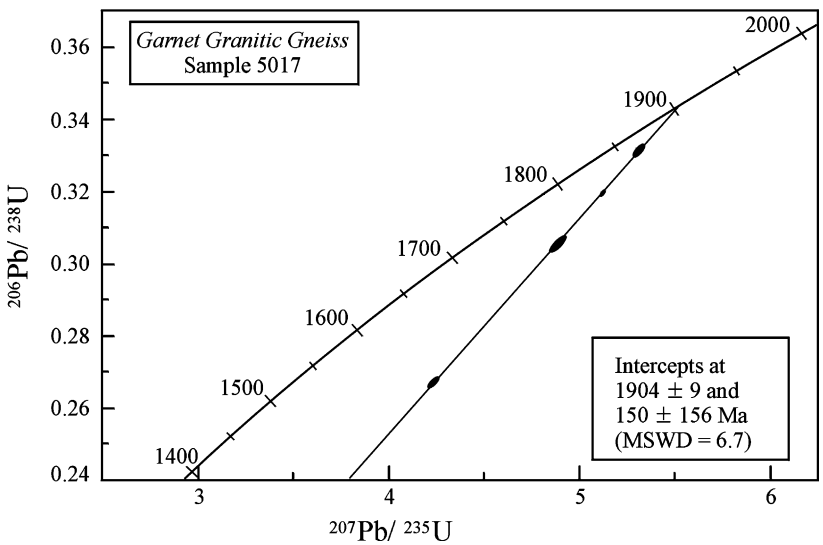

Fig. 9. Concordia diagram of zircon for the garnet granitic gneiss (sample 5017).

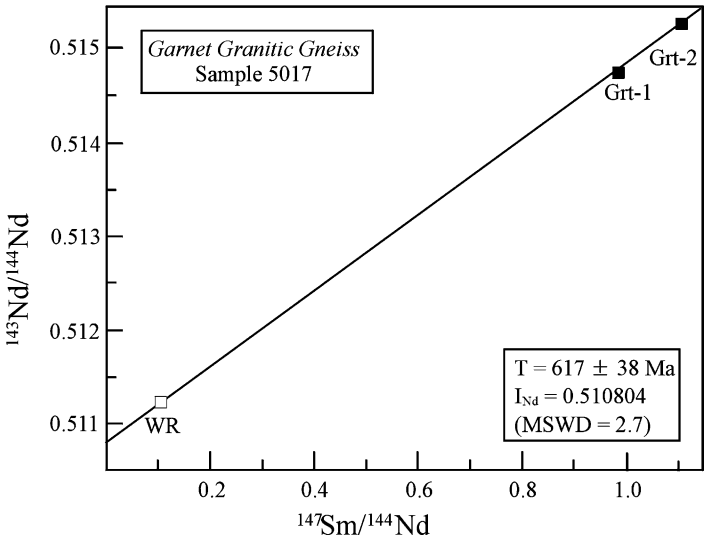

Fig. 10. $^{147}Sm/^{144}Nd$ vs. $^{143}Nd/^{144}Nd$ diagram for the garnet granitic gneiss (sample 5017).

and then dissolved with a mixed acid ($HF:HClO_4:HNO_3 = 4:1:1$) in Teflon vessels. REE fractions were collected by the conventional cation column chemistry. Sm and Nd fractions were separated from each other by the second step cation column chemistry using 0.2 M HIBA (α-hydroxy-*iso*-butyric acid) (Makishima et al., 1993). Isotopic ratios were measured using a VG54–30 thermal ionization mass spectrometer equipped with nine Faraday cups at the Korea Basic Science Institute. The Nd isotopic compositions were measured in dynamic mode. The $^{143}Nd/^{144}Nd$ ratios were normalized to $^{146}Nd/^{144}Nd = 0.7219$, and further corrected for Nd contribution from added spikes. Replicate analyses of La Jolla standard gave $^{143}Nd/^{144}Nd = 0.511843 \pm 0.000004$ ($n = 21$). Total blank levels were about 10 pg for Sm and 70 pg for Nd. Isochron parameters were calculated using the ISOPLOT program (ver. 2.71) of Ludwig (1994).

Whole rock and garnet Sm–Nd isotopic data are listed in Table 8 and plotted on an isochron diagram (Fig. 10). The Sm–Nd whole rock-garnet isochron age of garnet granitic gneiss is 617±38 Ma with MSWD of 2.7, and the T_{DM} of garnet granitic gneiss is 2.53 Ga. This Sm–Nd age is the youngest metamorphic age reported so far in the Yeongnam Massif. Kim (1999) reported a 1820 ± 11 Ma Sm–Nd age for peak metamorphism and a 1123 ± 22 Ma Rb–Sr biotite cooling age from a charnockite in the southwestern Yeongnam Massif. Park et al. (2000) also reported 1819–1717 Ma Sm–Nd metamorphic ages from gneisses and schists associated with the charnockite. Cheong et al. (2000) reported an age of 1840 ± 26 Ma using the Pb step leaching technique on garnet from the Wonnam Group in the northeastern Yeongnam Massif. Oh et al. (2000) reported Sm–Nd metamorphic ages of 1417 ± 52 and 1421 ± 14 Ma, respectively, from porphyroblastic gneiss and granitic gneiss in the southwestern Yeongnam Massif. Yi (2000) reported that CHIME zircon ages in granitic gneiss at the central part of the Yeongnam Massif were 2440, 2220, 1810 and 1450 Ma.

7. Discussion

The Punggi area of the northeastern Yeongnam Massif has undergone granulite-facies metamorphism (767–815 °C, 6.0–8.4 kb) followed by retrogression in the upper amphibolite facies (595–707 °C, 4.7–6.4 kb). The closure temperature of zircon for the U–Pb system is above 900 °C (Mezger and Krogstad, 1997) and the granulite-facies metamorphism of this area does not exceed 900 °C. Therefore, the 1904 ± 9 Ma of U–Pb zircon age appears to be the intrusion age of the igneous precursor to garnet granitic gneiss. The age is consistent with the intrusion ages of orthogneisses (2.1 and 1.9 Ga) in other parts of

Yeongnam Massif (Park et al., 1993; Turek and Kim, 1996; Cheong et al., 2000), suggesting widespread igneous activity between 2.1 and 1.9 Ga. However, the 617 Ma Sm–Nd garnet age obtained in the study area is not matched with the ca. 1.9–1.8 Ga metamorphic age suggested for the granulite-facies metamorphism in the Yeongnam Massif (Kim, 1999; Park et al., 2000; Kim and Cho, 2003).

Considering the closure temperature of the Sm–Nd system in garnet (e.g. 650 ± 30 °C, Mezger et al., 1992 or 700–750 °C, Hensen and Zhou, 1995), the Sm–Nd age most likely indicates the timing of upper amphibolite-facies metamorphism rather than granulite-facies metamorphism. However, Sagong et al. (2003) recently obtained another Sm–Nd garnet age of 956 ± 12 Ma from the study area, and suggested that apparent discrepancies in Sm–Nd garnet ages result from isotopic disequilibrium among garnet and other phases during the cooling stage. These authors further suggested that U–Pb or Pb–Pb systematics of garnet is far more useful to constrain the age of the granulite-facies metamorphism. Nevertheless, we interpret that the Sm–Nd garnet ages from the study area may result from late Proterozoic amphibolite-facies metamorphism. The late Proterozoic age was not reported in other parts of the Yeongnam Massif, and its significance needs to be further elucidated.

The North China Craton generally remained in a stable tectonic environment after high-pressure granulite-facies metamorphism at around 1.8 Ga and does not record younger metamorphic events (Zhai et al., 2000). Our ca. 617 Ma age for upper amphibolite-facies metamorphism, together with the 1.4 Ga metamorphic age (Oh et al., 2000; Yi, 2000) in other parts of the Yeongnam Massif, are different from metamorphic ages of North China Craton. Therefore, the tectonic model suggested by Yin and Nie (1993) in which the Yeongnam Massif is correlated with North China Craton, cannot be accepted until younger metamorphic event than 1.8 Ga is found in North China Craton.

The metamorphic age of granulite-facies metamorphism in the Hwacheon area, Gyeonggi Massif, is around 1.87 Ga (Lee et al., 2000). Based on similarities of the ages for the granulite-facies metamorphism, Park et al. (2000) and Cheong et al. (2000) suggested that the Yeongnam and Gyeonggi massifs are parts of the same tectonic unit. However, amphibolites in the Hongseong area, Gyeonggi Massif, have also undergone regional metamorphism at 290–260 Ma (Oh et al., 2001) or 223 ± 5 Ma (Cho, 2001) which can be correlated to a 249 ± 31 Ma event in the Samgot amphibolite, Imjingang belt (Ree et al., 1996). This Permo-Triassic event has not been recognized in the Yeongnam Massif. Thus, we conclude that two massifs underwent different metamorphic evolution and were not part of the same tectonic unit.

8. Conclusions

In the Punggi area, northeastern Yeongnam Massif:

1. The metamorphic grade increases from the amphibolite-facies zone to the granulite-facies zone (767–815 °C and 6.0–8.4 kb) towards the southeast.
2. The metamorphic rocks in the granulite-facies zone and the transitional zone between amphibolite to granulite facies were overprinted by upper amphibolite-facies retrograde metamorphism (595–707 °C and 4.7–6.4 kb).
3. The U–Pb zircon age of 1904 ± 9 Ma from a garnet granitic gneiss represents the emplacement age of its precursor, and corroborates a major magmatic activity at ca. 1.9 Ga in the Yeongnam Massif. A Sm–Nd whole rock-garnet age of 617 ± 38 Ma from the same sample is inferred to represent a late Proterozoic metamorphic event of upper amphibolite facies. Further studies are necessary to elucidate the implication of late Proterozoic ages, because they are not reported in other parts of the Yeongnam Massif.

Acknowledgements

We thank A. Indares, anonymous reviewer and co-guest editor M. Cho for critical comments that led to substantial changes and improvements in the manuscript. This work was supported by the Brain Korea 21 Project, and H.S. Kim also acknowledges the half-year sabbatical fund of 2001 at Korea University. We would like to thank to C.S. Cheong at the Korea Basic Science Institute (KBSI) for Sm–Nd isotope analyses, I.S. Choi in the Center for Mineral Resources Research (CMR) at Korea University for

electron microprobe analyses, and H.M. Li at Tianjin Institute of Geology and Mineral Resources for zircon analyses.

References

Berman, R.G., 1991. Thermobarometry using multiequilibrium calculations: a new technique, with petrological applications. Can. Miner. 29, 833–855.

Berman, R.G., Aranovich, L.Y., 1996. Optimized standard state and solution properties of minerals. I. Model calibration for olivine, orthopyroxene, cordierite, garnet, and ilmenite in the system FeO–MgO–CaO–Al_2O_3–TiO_2–SiO_2. Contrib. Miner. Petrol. 126, 1–24.

Chang, E.Z., 1996. Collision orogeny between north and South China and its eastern extension in the Korean Peninsula. J. SE Asian Earth Sci. 13, 267–277.

Cheong, C.S., Kown, S.-T., Park, K.-H., 2000. Pb and Nd isotopic constraints on Paleoproterozoic crustal evolution of the northeastern Yeongnam Massif, South Korea. Precambrian Res. 102, 207–220.

Cho, M., 2001. A continuation of Chinese ultrahigh-pressure belt in Korea: evidence from ion microprobe U–Pb zircon age. Gondwana Res. 4, 708.

Cluzel, D., Lee, G.-J., Cadet, J.P., 1991. Indosinian dextral ductile fault system and synkinematic plutonism in the southwest of the Ogcheon belt (South Korea). Tectonophysics 194, 131–151.

Eckert, J.O., Newton, R.C., Kleppa, O.J., 1991. The DH of reaction and recalibration of garnet-pyroxene-plagioclase-quartz geobarometers in the CMAS system by solution calorimetry. Am. Miner. 76, 148–160.

Ernst, W.G., Liou, J.G., 1995. Contrasting plate-tectonic styles of the Qinling–Dabie–Sulu and Franciscan metamorphic belts. Geology 23, 353–356.

Harley, S.L., 1984. An experimental study of the partitioning of Fe and Mg between garnet and orthopyroxene. Contrb. Miner. Petrol. 86, 359–373.

Hensen, B.J., Zhou, B., 1995. Retention of isotopic memory in garnets partially broken down during an overprinting granulite facies metamorphism: implications for the Sm–Nd closure temperature. Geology 23, 225–228.

Hoisch, T.D., 1990. Empirical calibration of six geobarometers for the mineral assemblage quartz + muscovite + biotite + plagioclase + garnet. Contrib. Miner. Petrol. 104, 225–234.

Kim, D.Y., 1999. Petrology, Geochemistry and Geochronology of Charnockite in the Southwestern Sobaeksan Massif, Korea. M.S. Thesis, Pukyong University Busan, Korea, 79 (in Korean with English Abstract).

Kim, J., Cho, M., 1999. Progressive low-pressure metamorphism in northeastern Yeongnam Massif, Korea. Geol. Soc. Korea, Abstr. Prog. 54, 76–77, abstract (in Korean).

Kim, J., Cho, M., 2003. Low-pressure metamorphism and leucogranite magmatism, northeastern Yeongnam Massif, Korea: implication for Paleoproterozoic crustal evolution. Precambrian Res. 122, 235–251.

Kim, K.H., Lee, J.D., Choi, M.O., 1992. Carboniferous-Triassic paleomagnetism of South Korea. J. Geomag. Geoeletr. 44, 959–978.

Koziol, A.M., Newton, R.C., 1988. Redetermination of the anorthite breakdown reaction and improvement of the plagioclase-garnet-Al_2SiO_5-quartz geobarometer. Am. Miner. 73, 216–223.

Kretz, R., 1983. Symbols for rock-forming minerals. Am. Miner. 68, 277–279.

Kwon, S.-T., Ree, J.-H., Park, K.-H., Jeon, E.-Y., 1995. Nature of contact between the Ogcheon belt and Yeongnam Massif and the Pb–Pb age of granitic gneiss in Cheondong-ri, Danyang. J. Petrol. Soc. Korea 4, 144–152 (in Korean with English abstract).

Kwon, Y.W., Kim, H.S., Oh, C.W., 1997. Polymetamorphism of the Odesan Gneiss Complex in the northeastern area of Kyonggi Massif. Korea. J. Petrol. Soc. Korea 6, 226–243 (in Korean with English abstract).

Lee, S.M., Na, K.C., Lee, S.H., Park, B.Y., Lee, S.W., 1981. Regional metamorphism of the metamorphic rock complex in the southeastern region of the Yeongnam Massif. J. Geol. Soc. Korea 17, 169–188 (in Korean with English abstract).

Lee, C.H., Lee, S.H., Chang, T.W., 1989. Geological report of the Punggi sheet (1:50,000). Korea. Inst. Energy Resources, 14.

Lee, S.R., Cho, M., Yi, K., Stern, R.A., 2000. Early Proterozoic granulites in central Korea: tectonic correlation with Chinese cratons. J. Geol. 108, 729–738.

Ludwig, K.R., 1994. ISOPLOT—A Plotting and Regression Program for Radiogenic Isotope Data. Version 2.71. USGS Open File Rep. 91, 445.

Makishima, A., Nakamura, E., Akimoto, S., Champbell, I.H., Hill, R.I., 1993. New constrains on the ^{138}La β-decay constant based on a geochronological study of the granites from the Yilgarn Block, Western Australia. Chem. Geol. 104, 293–300.

Mezger, K., Krogstad, E.J., 1997. Interpretation of discordant U–Pb zircon ages: an evaluation. J. Metam. Geol. 15, 127–140.

Mezger, K., Essene, E.J., Halliday, A.N., 1992. Closure temperatures of the Sm–Nd system in metamorphic garnets. Earth Planet. Sci. Lett. 113, 397–409.

Oh, C.W., Jeon, E.Y., Park, B.Y., Ahn, K.S., Lee, J.H., 2000. Metamorphic evolution of granitic and porphyroblastic gneisses in the Seungju–Suncheon area, the southwestern part of the Sobacksan Massif. J. Petrol. Soc. Korea 9, 121–141 (in Korean with English abstract).

Oh, C.W., Jeon, E.Y., Choi, S.K., Song, S.W., 2001. Late Paleozoic metamorphism and its tectonic implication of the metabasites and host rocks in the Baekdong area. Petrol. Soc. Korea, Abstr. Prog. 2001, 143–144 (in Korean).

Park, K.H., Cheong, C.S., Lee, K.S., Chang, H.W., 1993. Isotopic composition of lead in Precambrian granitic rocks of the Taebaeg area. J. Geol. Soc. Korea 29, 387–395 (in Korean with English abstract).

Park, K.H., Song, Y., Park, M., Lee, S., Ryoo, H., 2000. Petrological, geochemical and geochronological studies of Precambrian basement in northeast Asia region. 1. Age of the metamorphism of Jirisan area. J. Petrol. Soc. Korea 9, 29–39 (in Korean with English abstract).

Perchuk, L.L., Lavrent'eva, I.V., 1983. Experimental investigation of exchange equilibria in the system cordierite-garnet-biotite.

In: Saxena, S.K. (Ed.), Advances in Physical Geochemistry. Springer-Verlag, New York, pp. 111–130.

Ree, J.-H., Cho, M., Kwon, S.-T., Nakamura, E., 1996. Possible eastward extension of Chinese collision belt in South Korea: the Imjingang belt. Geology 24, 1071–1074.

Sagong, H., Cheong, C.S., Kwon, S.-T., 2003. Paleoproterozoic orogeny in South Korea: evidence from Sm–Nd and Pb step leaching garnet ages of Precambrian basement rocks. Precambrian Res. 122, 275–295.

Shin, B.W., Choi, S.I., 1968. Explanatory text of the geological map of Sangkumgok sheet (1:50,000). Geol. Survey Korea, 15.

Song, Y.S., 1999. Granulite xenoliths in porphyroblastic gneiss from Mt. Jiri area, SW Yeongnam Massif, Korea. J. Petrol. Soc. Korea 8, 34–45 (in Korean with English abstract).

Song, Y.S., Lee, S.M., 1989. Petrology of the Precambrian metamorphic rocks from the central Yeongnam Massif, Korea. J. Geol. Soc. Korea 25, 451–468 (in Korean with English abstract).

Spear, F.S., Kohn, M.J., Cheney, J.T., 1999. *P–T* paths from anatectic pelites. Contrib. Miner. Petrol. 134, 17–32.

Steiger, R.H., Jäger, E., 1977. Subcommission on geochronology: convention on the use of decay constants in geo- and cosmochronology. Earth Planet. Sci. Lett. 36, 359–362.

Tracy, R.J., 1982. Compositional zoning and inclusions in metamorphic minerals. Rev. Miner. 10, 355–397. In: Ferry, J.M. (Ed.), Characterization of Metamorphism Through Mineral Equilibria. Mineral. Soc. Am., pp. 355–397.

Turek, A., Kim, C.B., 1996. U–Pb zircon ages for Precambrian rocks in southwestern Gyeonggi massifs, Korea. Geochem. J. 30, 231–249.

Wang, Q., Ishiwatari, A., Zhao, Z.Y., Hirajima, T., Hiramatsu, N., Enami, M., Zhai, M., Li, J., Cong, B., 1993. Coesite-bearing granulite retrograded from eclogite in Weihai, eastern China. Eur. J. Miner. 5, 141–152.

Won, C.G., Lee, C.H., 1967. Explanatory text of the geological map of Danyang sheet (1:50,000). Geol. Survey Korea, 34.

Yao, Y., Ye, K., Liu, J., Cong, B., Wang, Q., 2000. A transitional eclogite- to high pressure granulite-facies overprint on coesite-eclogite at Taohang in the Sulu ultrahigh-pressure terrane, eastern China. Lithosphere 52, 109–120.

Yi, H.S., 2000. Zircon CHIME Age and Origin of the Precambrian Gneisses from Kimcheon Area in the Central Yeongnam Massif, Korea. M.S. Thesis, Pukyong University Busan, Korea, 101 (in Korean with English Abstract).

Yin, A., Nie, S., 1993. An indentation model for the North and South China collision and the development of the Tan-Lu and Honam fault systems, eastern Asia. Tectonics 12, 801–813.

Zhai, M., Cong, B., Guo, J., Liu, W., Li, Y., Wang, Q., 2000. Sm–Nd geochronology and petrography of garnet pyroxene granulites in the northern Sulu region of China and their geotectonic implication. Lithosphere 52, 23–33.

Zhang, R., Liou, J.G., Ernst, W.G., 1995. Ultrahigh-pressure metamorphism and decompression *P–T* paths of eclogites and country rocks from Weihai, eastern China. Island Arc. 4, 293–309.